JMEPEG (2005) 14:18-27
DOI: 10.1361/10599490522329

1059-9495/$19.00

Effect of Single and Duplex Aging on Precipitation Response, Microstructure, and Fatigue Crack Behavior in Al-Li-Cu Alloy AF/C-458

James Fragomeni, Robert Wheeler, and K.V. Jata

(Submitted March 29, 2004)

The interrelationships between precipitate characteristics and mechanical properties of Al-Li-Cu alloy AF/C-458 were quantified. The microstructure, precipitation response, and fatigue crack growth (FCG) rates in the Al-Li-Cu alloy AF/C-458 were studied following single and duplex aging treatments for varying aging times on specimens that were given a 6% stretch after solution heat treatment. The aging response was studied using hardness and compression yield strength measurements. Quantitative transmission electron microscopy methods were used to characterize average size, volume fraction, number density, and interparticle spacing of strengthening precipitates [i.e., δ′ (Al_3Li) and T_1 (Al_2CuLi)]. Strength and FCG rates for select heat treatments were obtained and were related to the precipitate microstructure and yield strength data.

Keywords aging, aluminum-lithium-copper, fatigue, hardness, microstructure, precipitation strengthening, quantitative microscopy

1. Introduction

Aluminum-lithium (Al-Li) alloys are used commercially in military aircraft and space vehicles in several critical applications. There is still, however, an interest in developing the next generation of Al-Li alloys with improved specific strength and damage tolerance and reduced mechanical property anisotropy. Recently, the U.S. Air Force and Aluminum Company of America (Alcoa) developed two aluminum-lithium-copper (Al-Li-Cu) alloys, designated AF/C-489 and AF/C-458 (Ref 1-5), with 2.1 and 1.8 wt.% Li, respectively. The AF/C-458 alloy has shown superior strength, damage tolerance (Ref 6), and stress corrosion cracking resistance (Ref 7, 8). Recently, studies by Csontos and Starke (Ref 4) and Csontos (Ref 5) compared precipitation and slip behavior between the AF/C-489 and AF/C-458 alloys by employing single and duplex aging. The authors concluded that the lower ductility in the AF/C-489 alloy compared with that in the AF/C-458 alloy is due to a large grain size, a higher volume fraction of the δ′ precipitates, and enhanced planar slip-and-stress concentration at grain boundaries. Thus, the AF/C-458 alloy has exhibited improved mechanical property benefits for aerospace structural applications compared with other Li-containing Al alloys (Ref 4).

The objective of this work was, in part, to understand the effect of artificial aging on the precipitate microstructure in the Al-1.8wt.%Li-2.7Cu-0.3Mg-0.5Zr-0.3Mn-0.8Zn (AF/C-458) alloy and to study the effects of aging on fatigue crack growth (FCG) rate. The Air Force Research Laboratory and ALCOA developed the alloy AF/C-458 to achieve an elongation >5% at the peak-strength condition. This alloy was a derivative of the previously developed Al-Li-Cu alloy AF/C-489 (Ref 9).

The precipitate characteristics are known to control the mechanical properties of age-hardened Al alloys (Ref 10-16). In this research, single and duplex aging studies were performed. In Al-Li alloys, stretching prior to a duplex aging schedule has been found to greatly increase the ductility and fracture toughness (Ref 17-20). Plastic deformation prior to aging enhances the precipitation response of Al-Li-Cu-X alloy AF/C-458 (Ref 4, 17, 18). The increase in the hardness and strength of the alloy by prestretching can be correlated to the microstructure precipitates (Ref 17). Duplex aging is expected to enhance the matrix precipitation of the T_1 (Al_2CuLi) intermetallic phase leading to accelerated overaging. The presence of well-distributed T_1 precipitates was seen throughout the matrix and contributed to the strength and hardness of the alloy. Transmission electron microscopy (TEM) was used to characterize the average size, distribution, morphology, volume fraction, number density, and interparticle spacing of various intermetallic precipitates. The δ′ and T_1 intermetallic precipitates were analyzed by quantitative microscopy methods for samples that had a 6% stretch and varying heat-treating conditions.

2. Precipitation Response

The microstructure of Al-Li alloy AF/C-458 was recently characterized by Csontos and Starke (Ref 4). The results of their study show that precipitation in the AF/C-458 alloy is similar to that in other Al-Li-Cu alloys. Various precipitates encountered in this alloy are briefly described below.

2.1 T_1 (Al_2LiCu) Phase

The crystal structure of the T_1 (Al_2LiCu) phase is known to have a hexagonal crystalline structure. The T_1 phase was ini-

James Fragomeni, The University of Detroit Mercy, College of Engineering & Science, Department of Mechanical Engineering, Detroit, MI; and **Robert Wheeler** and **K.V. Jata,** Air Force Research Laboratory, Materials and Manufacturing Directorate, Airforce Research Laboratory/Metals, Ceramics and Nondestructive Evaluation Division/ Materials and Manufacturing Directorate, 2230 Tenth Street, Wright Patterson Air Force Base, OH. Contact e-mail: jamesfrag@yahoo.com.

tially discovered by Hardy and Silcock (Ref 20), who determined its lattice parameters: $a = 0.4965$ nm and $c = 0.9345$ nm. Noble and Thompson (Ref 21) observed the formation of plate-shaped precipitates on {111} planes in ternary Al-Li-Cu alloys that were comparable to Alcoa alloys 2090 and C458. Noble and Thompson (Ref 21) identified these plate-shaped precipitates on {111} as the T_1 phase and also verified the orientation relationship originally proposed by Hardy and Silcock (Ref 20) as $\{0001\}_{T1}//\{111\}_{Al}$. The thin plates lie on {111} matrix planes, which means that three matrix slip planes intersect the plate at angles of 70.5° (Ref 19). The T_1 particles provide substantial strengthening to Al-Li-Cu alloys (Ref 13).

2.2 δ′ (Al_3Li) Phase

The δ′ (Al_3Li) precipitates are ordered, spherical, and coherent with the Al lattice, and they also nucleate and coarsen/grow homogeneously in the matrix. The δ′ phase has the ordered face-centered cubic (fcc) or $L1_2$ (Cu_3Au) superlattice crystal structure with a lattice parameter (a) equal to 0.404 ± 0.003 nm (Ref 23, 25). The cubic lattices of the δ′ particles and the Al matrix are geometrically similar, having a small misfit strain approximately equal to −0.08 ± 0.02% (Ref 22, 26, 27). The δ′ phase orientation is the same as the fcc matrix with $\{100\}_{\delta'}$ //$\{100\}_{Al}$.

2.3 Al_3Li/Al_3Zr Composite Precipitates

Zirconium additions to Al-Li alloys form the dispersoid β′ (Al_3Zr), which substantially decreases the recrystallization of grains during ingot breakdown and hot rolling. The composite precipitates contain an inner core of β′ surrounded by an outer shell of the δ′, which resemble a ring-shaped or doughnut-shaped spherical particle (Ref 28, 29).

2.4 Al_3Li/Al_2Cu Composite Precipitates

The θ′ (Al_2Cu) phase is not reported to be a stable phase in the AF/C-458 alloy. When found in similar alloys, these precipitates lie on {001} habit planes. Their shape is that of very thin discs that are coherent with the aluminum matrix, producing a strain field that contributes to the effectiveness of this precipitate as a strengthening dispersion in many Al-Cu base alloys. The coprecipitation of θ′ with δ′ has been observed in underaged alloys (Ref 28, 29).

3. Experimental

3.1 Hardness Measurements

AF/C-458 plate material was obtained from Alcoa in the T3 temper. The plate had a 6% stretch after solution heat treatment. Samples were machined from the plate and artificially aged using both single and duplex aging practices. Heat treatments were carried out on 25 mm square coupons in ambient air. These coupons were quenched directly from the aging furnace into a water bath. A number of test coupons were aged at 150 °C for various times, and Rockwell B hardness measurements recorded. Hardness readings were made along the short transverse direction with parallel surfaces ground to a 600-grit finish. After determining the peak age condition at 150 °C, a number of coupons were given duplex heat treatments consisting of the shortest time to achieve the peak age hardness at 150 °C followed by various aging times at 190 °C. Precipitation hardening due to aging was followed by hardness and compression yield strength measurements. The artificial aging response was evaluated from hardness measurements.

3.2 Transmission Electron Microscopy

The average size, distribution, number density, volume fraction, and spacing of the δ′ (Al_3Li) and T_1 (Al_2LiCu) precipitates were directly measured from TEM dark-field images. The volume fraction was calculated based on the TEM foil thickness and average precipitates size.

TEM analysis was carried out on a Philips CM200 instrument (Amsterdam, the Netherlands) equipped with a field-emission gun. Thin-foil specimens were prepared by electropolishing 3 mm diameter discs in a solution of 5% perchloric acid in methanol at a temperature of −40 °C. Both bright-field and dark-field images were recorded from each sample with the grain of interest oriented near ⟨110⟩. The foil thickness determination required for the quantification of particle volume fractions and densities were measured using the fringe image of inclined T_1 particles belonging to other variants of this precipitate.

3.3 Particle Size Measurements

Particle size measurements were made for both T_1 and δ′ precipitates directly from TEM images. Projected images of the actual particle sizes were measured. Based on standard quantitative microscopy theory and methods, the measurements of the projected images were converted to actual particle sizes. Two projected particle diameter-size images were measured directly from the TEM micrographs for each particle. Thus, an average size and aspect ratio was determined for each individual particle of the entire distribution of particle sizes. For the nonspherical T_1 particles, size distribution histograms were determined from the size measurements. The average particle size was also determined based on the measurements of the projected particle images.

4. Results

4.1 Optical Microstructures, Hardness, and Yield Strength

The optical microstructure of the alloy AF/C-458 in rolled plate form is shown in Fig. 1. This figure illustrates the conventional pancake-shaped grains observed in Al-Li alloy plate products. The aging response of the AF/C-458 plate, determined from hardness measurements, is given in Fig. 2. Closed circles indicate the Rockwell B hardness of samples isothermally aged at 150 °C as a function of time. The open squares represent samples given an initial 24 h heat treatment at 150 °C followed by aging for additional times at 190 °C. Here, times are given as a total of the 24 h at 150 °C plus the additional time at 190 °C. Data in Fig. 2 shows that, even with duplex aging, the hardness loss in the AF/C-458 alloy is minimal. Compressive buckling strengths obtained as a function of aging

time are also shown in this figure and are indicated by filled triangles.

The precipitate phases that were observed included δ′ (Al_3Li), T_1 (Al_2LiCu), β′ (Al_3Zr), and θ′ (Al_2Cu). For all of the aging times studied here, the composite Al_3Zr/Al_3Li particles were found to be much larger in size than the δ′, but were much fewer in number density than the δ′ precipitates. In this article, only observations of the T_1 and δ′ precipitates are quantified and discussed.

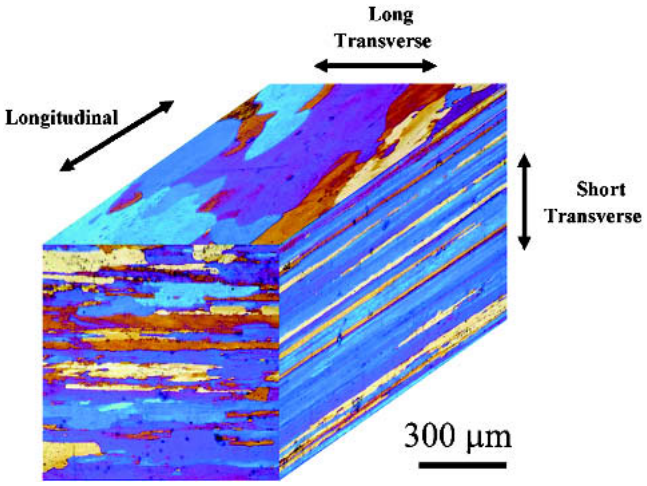

Fig. 1 Optical microstructure of the ¾ in. plate of the Al alloy AF/C-458

4.2 Microstructure of Sample Aged at 150 °C for 3 h

Figure 3(a) shows a bright-field image of the uniform distribution of dislocations across a 2 μm^2 section of the microstructure. The selected area diffraction (SAD) pattern in Fig. 3(b) does not contain the streaking usually associated with the T_1 phase. However, some degree of diffusivity is present, suggesting the existence of very early-stage nucleation of precipitates related to the line defects, as reported in the literature. The δ′ particles are very fine in Fig. 3(b) with a high number density. Strong superlattice intensity consistent with the $L1_2$ ordering of this phase is present in the diffraction pattern. Finally, under weak beam-imaging conditions (not shown), a high density of dislocations is evident, but T_1 has not begun to nucleate. Higher-magnification imaging would be required to resolve such events.

4.3 Microstructure of Samples Aged at 150 °C for 24 h

The microstructure for this aging condition (peak aging) is shown in Fig. 4. Coarsening of the δ′ phase in Fig. 4(a), and the nucleation and growth of T_1 particles in Fig. 4(b) has occurred, as can be seen by comparing the TEM micrographs in Fig. 3 for the sample aged for 3 h. The [110] diffraction pattern now indicates well-developed streaking along $g = 111$ vectors related to the thin T_1 particles. These were absent in the pattern from the sample aged for 3 h. It should be noted that each δ′ precipitate now coexists with a very thin plate of θ′. Because the habit plane for θ′ is {001} and the images are recorded near [110], only one variant of these discs is visi-

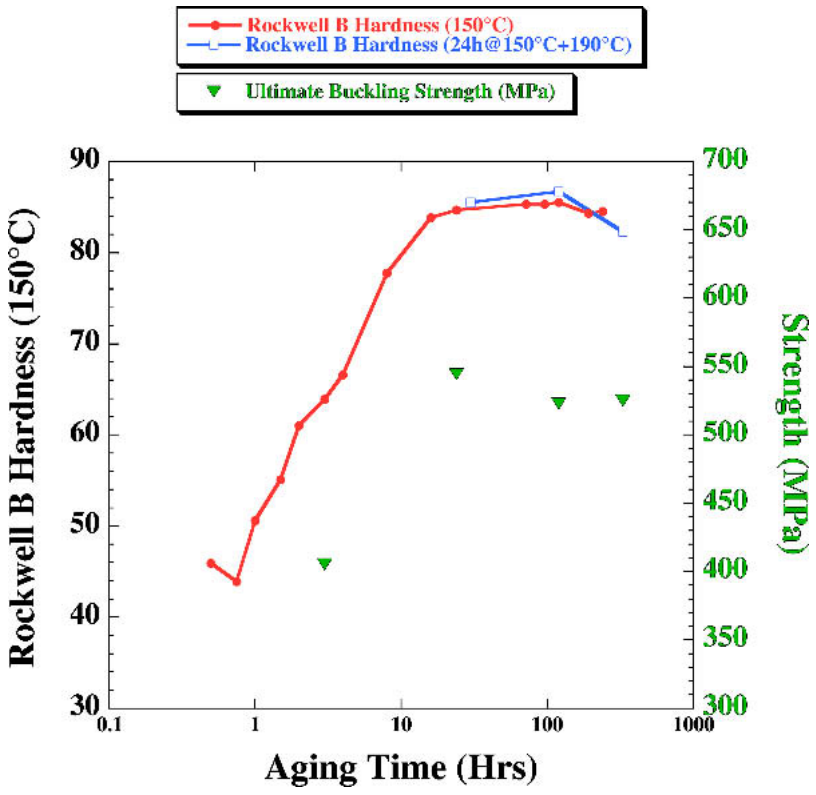

Fig. 2 Hardness of the AF/C-458 alloy as a function of single and duplex aging

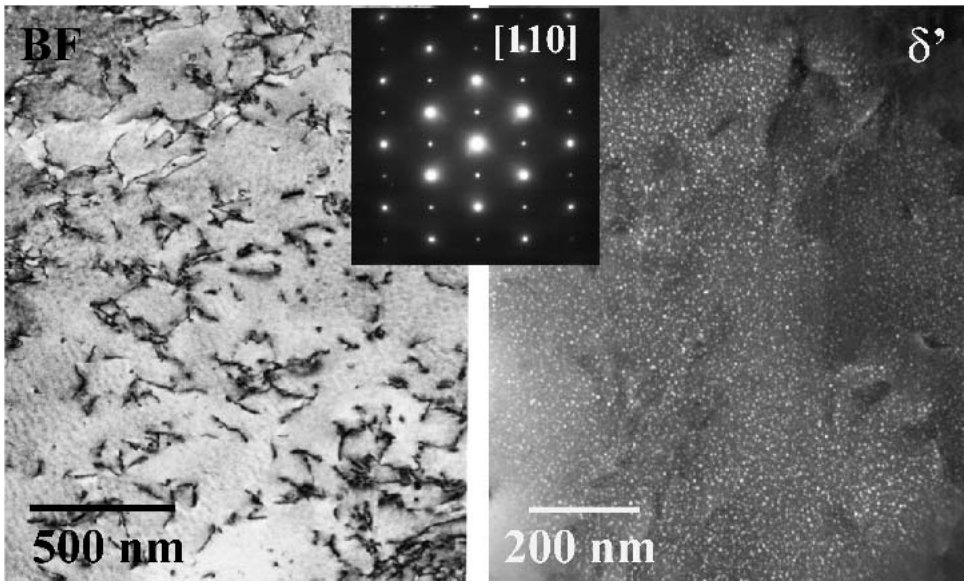

Fig. 3 TEM micrographs of the AF/C-458 sample aged for 3 h at 150 °C showing (a) a bright-field image of dislocation segments and (b) a dark-field image of δ′ precipitates. The insert is a [110] diffraction pattern with {1100} superlattice intensity used to image the δ′ particle.

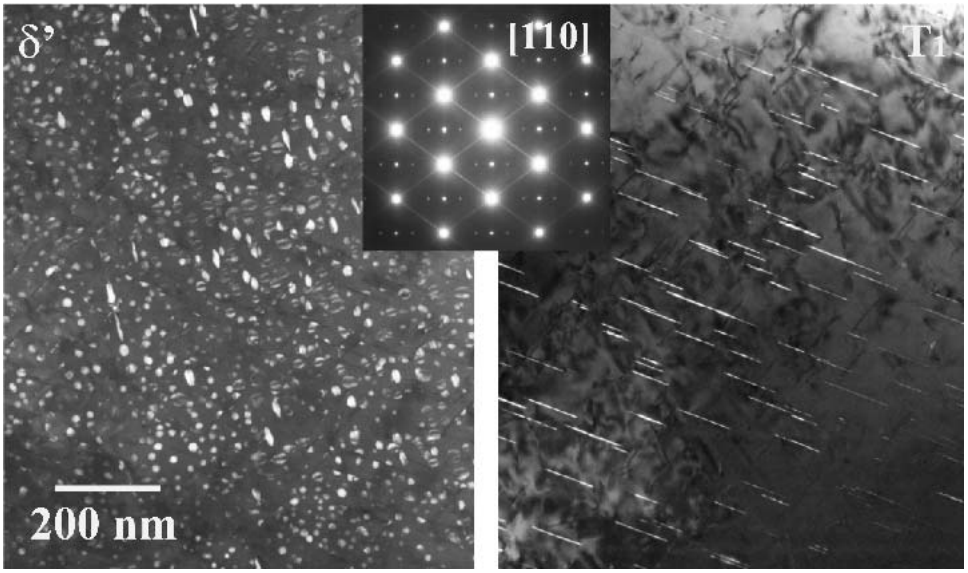

Fig. 4 Dark-field TEM micrographs and the associated [110] diffraction pattern for the Al-Li-Cu AF/C 458 alloy aged at 150 °C for 24 h. (a) δ′ Al_3Li precipitates. (b) T_1 Al_2LiCi precipitates

ble "edge-on." Close examination of the δ′ particles in Fig. 4 indicates that about one-third of these precipitates have the characteristic midline feature, oriented nearly along the vertical direction in the image. The other two-thirds of the particles have a broad dark band that is oriented perpendicular to the θ′ discs lying on (001). This image contrast results from the remaining two orientations of θ′ discs. These lie on (100) and (010) planes, which are inclined at 45° to the [110] electron beam direction. The thin "rib" of θ′ within the δ′ precipitate does not persist at the longer aging times discussed below.

4.4 Microstructure of Duplex-Aged Samples

Long aging times at 150 °C did not decrease the hardness, as illustrated in Fig. 2. Hence, a duplex aging treatment was implemented to promote overaging. This consisted of initial aging of the samples at 150 °C for 24 h (peak age condition) followed by an additional treatment for various times at 190 °C. It is interesting to note from Fig. 2 that these subsequent long aging times at 190 °C caused little change in hardness once the peak age microstructure was established. Direct aging at 190 °C has been reported to achieve significantly

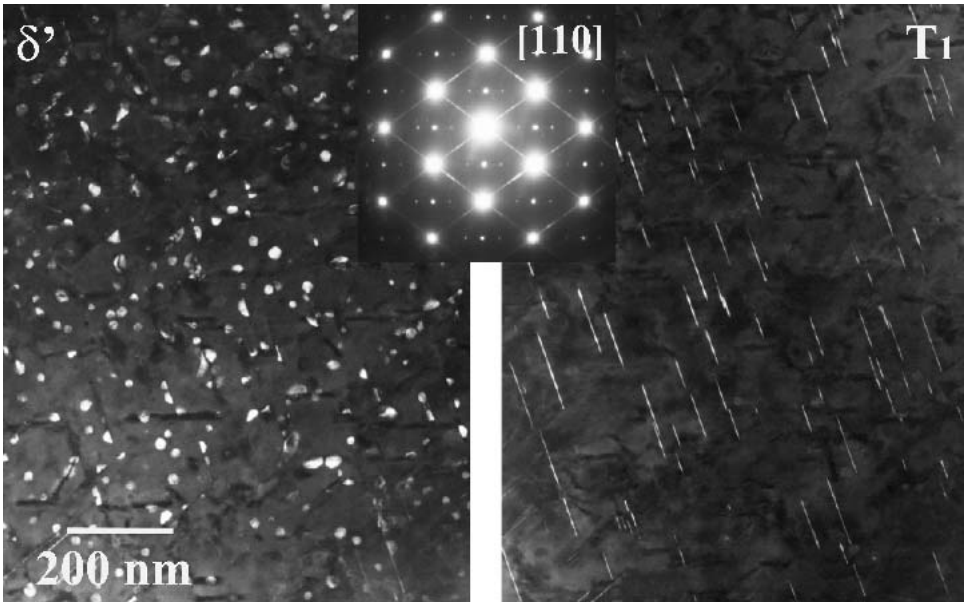

Fig. 5 TEM dark-field images and the associated diffraction pattern showing coarsening of the (a) δ′ particles and (b) T_1 precipitates after aging at 150 °C for 24 h followed by aging at 190 °C for 96 h

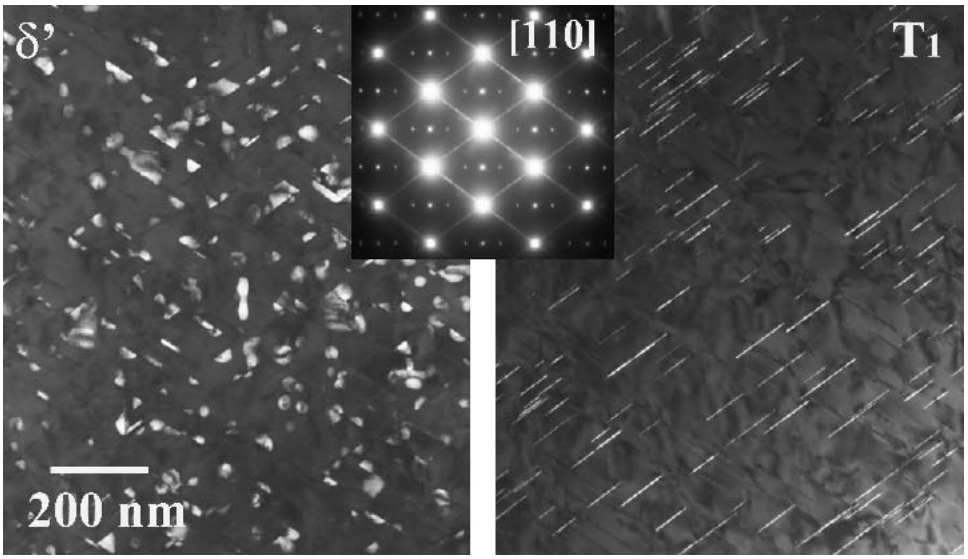

Fig. 6 TEM dark-field images and the associated diffraction pattern showing coarsening of the (a) δ′ particles and (b) T_1 precipitates after aging at 150 °C for 24 h followed by aging at 190 °C for 316 h

reduced strength and rapid overaging (Ref 4, 5). Hence, it would be expected that the microstructures would coarsen and that overaging would take place. Figure 5 shows the precipitate structure of the duplex-aged sample, given secondary aging for 96 h at 190 °C. Here, the δ′ particles have coarsened, and the θ′ ribs within them have dissolved. For the T_1 particles, quantitative changes from the peak-age microstructure are not so clear. Particle separation has also increased noticeably for the δ′ precipitates, and they are largely found in contact with T_1 plates.

From Fig. 6, further aging at 190 °C for 316 h results in a microstructure composed entirely of δ′ precipitates in contact with T_1 precipitates. While the size of the δ′ particles is clearly greater than that in the previous aging condition, any change in T_1 size is not obvious. The shape of the δ′ precipitates is no longer spherical because they are growing in contact with the flat surfaces of the T_1 platelets. The morphologies of the two dispersed strengthening phases are no longer simple and cannot be considered to be discretely dispersed.

4.5 Quantitative TEM Microscopy

The experimentally measured planar particle sizes were converted into true particles sizes that were determined using

quantitative stereology (Ref 24, 30-35) based on the TEM foil thickness, and the area and number densities of precipitates. The precipitate phases that were observed included δ′ (Al_3Li), T_1 (Al_2LiCu), β′ (Al_3Zr), and θ′ (Al_2Cu). Only δ′ and T_1 particles have been quantified here because these are the dominant precipitate phases in this alloy.

4.6 Quantitative Microscopy Measurements and Analysis

The harmonic diameters were tabulated from the planar particle size measurements of the δ′ and T_1 precipitates because the harmonic diameters can be used to correlate with particle size. The harmonic diameter is inversely equal to the sum of the reciprocals of the measured diameters divided by the total number of measured diameters. The harmonic diameters were calculated using the expression given by Underwood (Ref 30):

$$D_h = \frac{1}{\left(\sum \frac{N_i}{D_i}\right)\left(\frac{1}{\sum N_i}\right)} \quad \text{(Eq 1)}$$

where D_h is the harmonic average particle-size diameter and N_i is the number of particles for a given particle-size diameter. The reciprocal relationship can be seen more readily in the form (Ref 30):

$$\frac{1}{D_h} = \frac{(N_1 + N_2 + N_3 + \ldots + N_N)}{\left(\frac{N_1}{D_1} + \frac{N_2}{D_2} + \frac{N_3}{D_3} + \ldots + \frac{N_N}{D_N}\right)} \quad \text{(Eq 2)}$$

The volume fraction of the precipitates in the microstructure was also calculated from the experimental data. For the δ′ precipitates, overlapping and truncation effects were incorporated into the calculations. However, for T_1, only the truncation effect was included in the volume fraction determinations because the overlapping was not evident. For spherical particles of diameter, D, both overlapping and truncation were taken into account through the use of (Ref 30):

$$f_{\delta'} = -2 \ln (1 - A)\left(\frac{D}{D + 3t}\right) \quad \text{(Eq 3)}$$

where $f_{\delta'}$ is the volume fraction of δ′ precipitates, D is the average particle-size diameter, A is the projected area fraction measured from the dark-field TEM micrographs, and t is the TEM foil thickness. For the situation in which there are very large spherical particles in the overaged alloys, the effect of particle overlapping is small. However, the effect of truncation at the foil surface needs to be considered. Thus, for foil truncation only, Eq 3 becomes (Ref 30):

$$f_{\delta'} = \frac{2\,D\,A}{(2D + 3t)} \quad \text{(Eq 4)}$$

For the T_1 precipitates, the particle overlapping is very small and subsequently not important, so only the truncation effect needs to be considered. The T_1 precipitates are disk-shaped (not spherical), and, considering the measured planar length of the T_1 precipitates, the expression for the T_1 volume fraction can be written as:

$$f_{T_1} = \frac{(4\,A_{pl} \cdot N_{total})}{A_{total}}\left(\frac{2l_{pl}}{2l_{pl} + 3t}\right) \quad \text{(Eq 5)}$$

where l_{pl} is the experimentally measured planar length of the T_1 precipitates, N_{total} is the total number of precipitates on the measured plane of TEM image area, t is the TEM foil thickness, A_{total} is the total area of the microstructure field of view from which the particles are being measured, and A_{pl} is the experimentally measured planar particle area. For the T_1 precipitates, A_{pl} can be expressed as:

$$A_{pl} = l_{pl}\, w_{pl} \quad \text{(Eq 6)}$$

where w_{pl} is the experimentally measured planar particle width of the T_1 precipitates and l_{pl} is the experimentally measured planar length of the T_1 precipitates.

The edge effect was also taken into account when doing the particle size measurements for the planar particle size areas with respect to particles extending beyond the field of view. The edge effects were incorporated using the expression (Ref 30):

$$N_{total} = \frac{\left(N'' + \frac{N'}{2}\right)}{A_{total}} \quad \text{(Eq 7)}$$

where N' is the number of particles intersected by the edges of the field of the microstructure, N'' is the number of particles lying in the field of view of the microstructural area of interest, A_{total} is the total area of the microstructure field of view from which the particles are being measured, and N_{total} is the total number of particles corrected for the edge effect within the microstructural image area of interest.

Based on the harmonic diameters and the foil thickness, the number of particles per unit volume (i.e., the volume number density of the precipitates) can be determined. The volume number density can be determined using (Ref 31):

$$N_{volume} = N_{total}\frac{1}{\left(t + \frac{\pi\, D_h}{2}\right)} \quad \text{(Eq 8)}$$

where N_{volume} is the total number of intermetallic precipitate particle per unit volume and t is the thin foil thickness. Thus, based on the volume number density of precipitates, the true particle-size diameter can be predicted from (Ref 31):

$$D_{true} = \left(\frac{N_{total}}{N_{volume}}\right) - t \quad \text{(Eq 9)}$$

where D_{true} is the actual true average particle-size diameter for the distribution of intermetallic precipitate particles within the microstructure. For a very small area of the thin foil, the true particle-size diameter can be estimated using:

Table 1 Quantitative microstructure particle size data for δ′ precipitates for both single and duplex aged AF/C458 alloy samples, 6% prestretched before aging

Aging temperature, °C	Aging time, h	r_{planar}, nm	No. of particles measured	Average aspect ratio	Spherical morphology, %	TEM foil thickness, nm	Harmonic diameter, nm
150	3	4.1	18	0.778	45.5	20	4.1
	24	8.3	34	0.720	42.9	22	10.2
150 and 190(a)	24 and 96(a)	7.8	34	0.717	42.2	11	15.3
	24 and 316(a)	12.9	242	…	…	25	18.8

(a) Duplex aged

Table 2 Calculated quantitative microstructure particle size data for δ′ precipitates for both single and duplex aged AF/C458 alloy samples, 6% prestretched before aging

Aging temperature, °C	Aging time, h	N_A, nm^{-2}	N_{volume}, nm^{-3}	TEM foil thickness, nm	Volume fraction with overlap and truncation	D_{true}, nm	Average interparticle spacing, nm
150	3	11.8×10^{-3}	4.4×10^{-4}	20	0.0243	6.5	22
	24	19.0×10^{-4}	5.0×10^{-5}	22	0.0912	16.0	36
150 and 190(a)	24 and 96(a)	3.8×10^{-4}	1.1×10^{-5}	11	0.0470	24.0	88
	24 and 316(a)	3.1×10^{-4}	5.6×10^{-5}	25	0.0912	29.5	114

(a) Duplex aged

Table 3 Quantitative microstructure particle size data for T_1 precipitates for both single and duplex aged AF/C458 alloy samples, 6% prestretched before aging

Aging temperature, °C	Aging time, h	l_{planar}, nm	Width, nm	No. of particles measured	TEM foil thickness, nm	Harmonic length, nm	l_{planar} SD, nm
150	24	68.5	4.3	163	22	35.4	33.6
150 and 190(a)	24 and 96(a)	61.4	4.2	117	11	32.8	26.9
	24 and 316(a)	75.4	6.3	294	25	43.5	38.9
	24 and 316(a)	89.4	6.3	310	25	45.2	41.5

(a) Duplex aged

$$D_{true} = \left(\frac{N_{total}}{N_{volume}}\right) = \left(\frac{\pi}{2}\right) D_h \quad \text{(Eq 10)}$$

where D_h is the harmonic average particle-size diameter.

The harmonic diameter (Ref 30) is used to convert the experimentally measured planar particle sizes to actual true particle sizes. Thus, the harmonic diameter is very important in determining the true average particle size for a distribution of particle sizes.

4.7 Quantitative TEM

Tables 1 to 4 summarize the experimental quantitative measurements and the calculated microstructure parameters for the Al-Li-Cu AF/C-458 alloy. Tables 1 and 2 contain data for the δ′ precipitates. Tables 3 and 4 show data for the T_1 precipitates.

The general trend, given the limited aging data shown in Fig. 7, is for the volume fraction of δ′ to decrease while the T_1 volume fraction increases with aging time. This is consistent with the depletion of Li from the δ′ phase to accommodate the growth of T_1. The extent of this transfer of Li would then be limited only by Cu availability. After all excess Cu has been depleted from the nonequilibrium θ′ phase, and from the matrix, the volume fraction of the two phases will reach equilibrium. (This is because, after 24 h, θ′ is seen as a midrib on the δ′ precipitates.)

In Fig. 8, the number density of T_1 decreases slowly from a peak value near 24 h of aging. This indicates great thermodynamic stability of the T_1 phase once a sufficient particle size is achieved. Specifically, this size results in a continuous skeleton of interconnected T_1 platelets. The connectivity of the T_1 particles can be deduced from the observation that the particle size and center-to-center spacing, shown in Fig. 9 and 10, respectively, are equal (i.e., each are approximately 50 nm). In contrast, the δ′ size changes rapidly, while the precipitates remain relatively discrete (i.e., for aging times <96 h for the duplex heat treatment). At longer aging times, contact made with T_1 particles may contribute to slower rates of change in the size of δ′ particles.

Table 4 Calculated quantitative microstructure particle size data for T_1 precipitates for both single and duplex aged AF/C458 alloy samples, 6% prestretched before aging

Aging temperature, °C	Aging time, h	Area No. density, nm^{-2}	Vol. No. density, nm^{-3}	TEM foil thickness, nm	D_{true}, nm	Volume fraction without truncation	Volume fraction with truncation
150	24	6.9×10^{-4}	8.9×10^{-5}	22	55.6	0.271	0.0749
150 and 190(a)	24 and 96(a)	4.9×10^{-4}	7.8×10^{-5}	11	51.5	0.483	0.0869
	24 and 316(a)	6.4×10^{-4}	6.8×10^{-4}	25	68.3	0.679	0.0706
	24 and 316(a)	7.1×10^{-4}	7.4×10^{-4}	25	71.0	0.784	0.0766

(a) Duplex aged

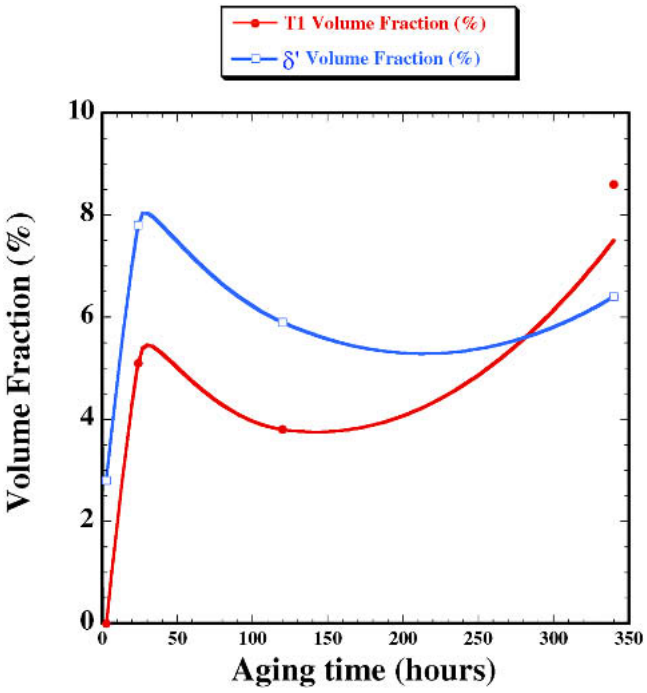

Fig. 7 Volume fraction of the T_1 Al_2LiCu precipitates and the Al_3Li precipitates as a function of single and duplex aging treatments on the Al-Li-Cu alloy AF/C-458

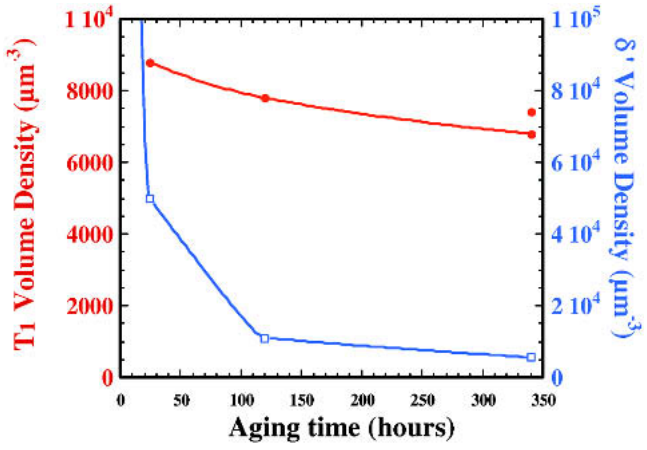

Fig. 8 The volume densities of the T_1 Al_2LiCu precipitates and the Al_3Li precipitates as a function of single and duplex aging conditions of the Al-Li-Cu alloy AF/C-458

4.8 FCG Rates

FCG rates for the single and duplex aging treatments were obtained for $R = 0.1$ at 30 Hz in laboratory air. FCG results show that the underaged alloy has the best crack growth resistance with the most overaged condition showing the least crack growth.

5. Discussion

Quantitative electron microscopy has been used to study the changes in the average size, distribution, morphology, volume fraction, number density, and interparticle spacing of various intermetallic precipitates that define the microstructure and control the properties of the AF/C-458 plate. As reported elsewhere, an incubation period is required prior to the nucleation and growth of the T_1 precipitates. Hence, the short-term aging response is governed entirely by the precipitation of δ′. At some point between 3 and 24 h at 150 °C, the finest distributions of T_1 precipitates are formed and undergo rapid coarsening. Aging beyond 24 h at 190 °C has relatively little effect on all quantifiable microstructural parameters shown in Fig. 6 to 10. These results indicate that duplex aging did not adversely affect the microstructure, hardness, or compression strength of the AF/C-458 alloy. As seen from Fig. 2, the hardness increased with aging up to 10 h and then was relatively constant after that. The compression strength also increased with aging up to 10 h and then remained relatively constant, showing only a slight decrease. With the given precipitate microstructure, as compared with single aging, duplex aging resulted in larger particle sizes and greater interparticle spacing for the δ′ and T_1 precipitates. When going from single aging (150 °C/24 h) to duplex aging (150 °C/24 h and 190 °C/96 h), the particle size increased by about 50% and the interparticle spacing was about 2.5 times larger for the δ′ precipitates. Further duplex aging from 150 °C/24 h to 190 °C/316 h resulted in a greater increase in both size and spacing (see Table 4). However, the T_1 precipitates showed much smaller increase as a consequence of the duplex aging (see Table 4 and Fig. 8). For the δ′ precipitates, both particle overlapping and particle-truncation effects were incorporated in the quantitative analysis. However, with T_1 precipitates only truncation effects were included in the analysis because particle overlapping was not seen with T_1 precipitates as compared to single aging. The volume number densities of both T_1 and δ′ were seen to decrease as a consequence of the duplex aging (Table 4 and Fig. 8). As seen from Fig. 8, there

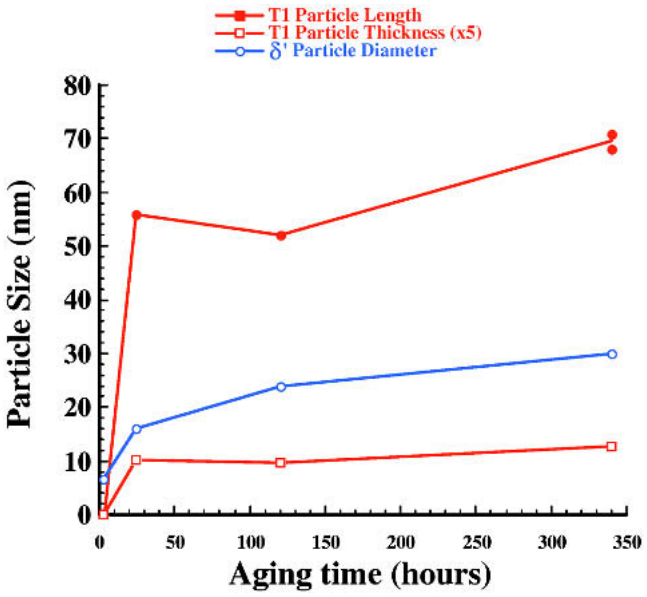

Fig. 9 Particle-size results for the T_1 Al_2LiCu precipitates, and the Al_3Li precipitates as a function of single and duplex aging conditions of the Al-Li-Cu alloy AF/C-458

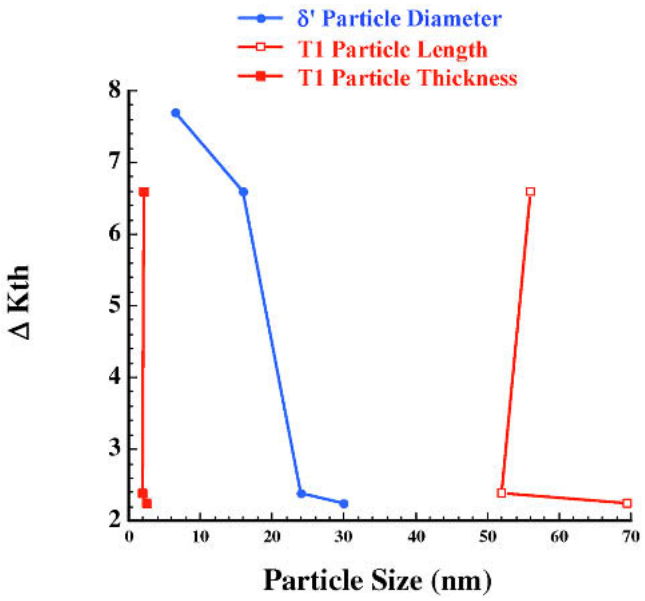

Fig. 11 The relationship between particle diameter and fatigue-crack threshold for the four aged Al-Li-Cu AF/C-458 samples

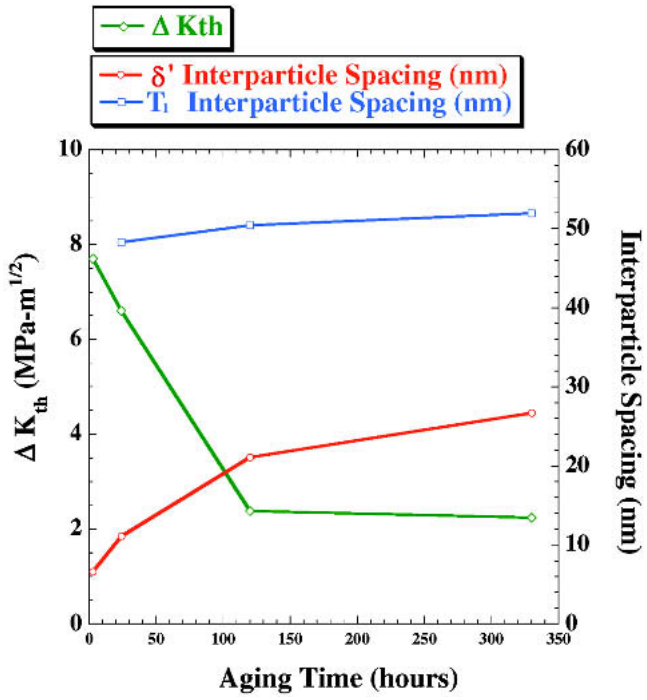

Fig. 10 Fatigue threshold and precipitate interparticle spacing of Al-Li-Cu alloy AF/C-458 as a function of aging time, fatigue threshold as a function of interparticle spacing, and fatigue threshold as a function of precipitate diameter

was a greater decrease in the volume number densities of δ′ particles than in the T_1 particles with aging.

Fatigue thresholds and interparticle spacing in this Al-Li alloy system are shown as a function of aging time in Fig. 10. The dependence of fatigue thresholds for various aging treatments is also shown as a function of particle size in Fig. 11. These graphs show that the most significant variation in FCG thresholds is observed for the δ′ particle. Neither the T_1 particle size nor the spacing appears to significantly affect the fatigue threshold for the aging conditions studied here. However, as δ′ particle size decreases, a higher fatigue threshold is observed. This is consistent with observations on the effects of particle shearing and bypassing on fatigue thresholds in Al-Li-Cu alloys (Ref 36, 37). It has been shown in the literature that when precipitates are coherent and the precipitate diameter is less than a critical size, precipitates are sheared by dislocations resulting in slip planarity. When the precipitate diameter exceeds the critical diameter, dislocation looping takes over. Planar slip increases reversible slip at the crack tip, and crack deflection (or crack path) is more tortuous (Ref 32). Both of these factors contribute to the slower FCG rates in the alloys aged for less time. On the other hand, when the deformation mechanism changes to having more homogeneous slip, irreversible slip is accumulated at the crack tip, and faster crack growth rates can be expected. A much flatter fracture path (or lower crack path deflections) accompanies this.

6. Conclusions

The microstructural features of an AF/C-458 alloy were characterized to determine the average size, distribution, number density, spacing, and volume fraction of δ′ and T_1 particles. Four aging treatments were used to quantify microstructure and precipitate characteristics with the FCG thresholds. As aging progressed, the interparticle spacing between the δ′ particles and the precipitate diameter increased more significantly than

did those for the T_1 particles. FCG results on AF/C-458 alloy are consistent with the observation of the fatigue threshold being higher for conditions of planar slip. The aging conditions used here suggest that δ′ particles may have a stronger effect on FCG than the T_1 precipitates. However, work is being carried out to validate these results for a broader aging window.

Acknowledgment

The material used for this study was fabricated, cast, and rolled by ALCOA, and the precipitation was aged and stretched by the Air Force Research Laboratory.

References

1. A. K. Hopkins, K.V. Jata, and R.J. Rioja, Isotropic Wrought Aluminum-Lithium Plate Development Technology, *Mater. Sci. Forum,* Vol 217-222, 1996, p 421-426
2. K.V. Jata, A. K. Hopkins, and R.J. Rioja, The Anisotropy and Texture of Al-Li Alloys, *Mater. Sci. Forum,* Vol 217-222, 1996, p 647-652
3. V.K. Jain, K.V. Jata, R.J. Rioja, J.T. Morgan, and A.K. Hopkins, Processing of an Experimental Aluminum-Lithium Alloy for Controlled Microstructure, *J. Mater. Proc. Technol.,* Vol 73, 1998, p 108-118
4. A.A. Csontos and E.A. Starke, Jr., The Effect of Processing and Microstructure Development on the Slip and Fracture Behavior of the 2.1 Wt Pct Li AF/C-489 and 1.8 Wt Pct Li AF/C-458 Al-Li-Cu-X Alloys, *Metall. Mater. Trans. A,* Vol 31A, 2000, p 1965-1976
5. A.A. Csontos, "Microstructural Effects on the Slip and Fracture Behavior of Isotropic Al-Li-Cu-X Alloys," Ph.D. dissertation, University of Virginia, 2001
6. K.V. Jata, Ed., Aluminum-Lithium Alloys, Aluminum-Lithium Workshop Report, Bass Lake Lodge, Wright-Patterson Air Force Base, OH, Materials Directorate, WPAFB, Aug 1998, p 1-238
7. D. Mathur, "Localized Corrosion and Stress Corrosion Cracking Studies of Al-Li-Cu Alloy AF/C-458," M.S. thesis, Ohio State University, 2000
8. J.E. Kertz, P.I. Gouma, and R.G. Buchheit, Localized Corrosion Susceptibility of Al-Li-Cu-Mg-Zn Alloy AF/C458 Due to Interrupted Quenching from Solutionizing Temperatures, *Metall. Mater. Trans. A,* Vol 32A (No. 10), 2001, p 2561A-2573A
9. V.K. Jain, K.V. Jata, R.J. Rioja, J.T. Morgan, and A.K. Hopkins, Processing of an Experimental Aluminum-Lithium Alloy for Controlled Microstructure, *J. Mater. Proc. Technol.,* Vol 73, 1998, p 108-118
10. W. Cassada, "Heterogeneous Precipitation in Al-Li-Cu Alloys," Ph.D. dissertation, University of Virginia, 1987
11. C.P. Blankenship, "Optimizing Mechanical Properties in Al-Li-X Alloys by Microstructural Design," University of Virginia, 1992
12. M. Tamura, T. Mori, and T. Nakamura, Precipitation of Al_3Li from an Al-3.0wt.%Li Alloy and Some Properties of Al_3Li, *J. Jpn. Inst. Met.,* Vol 34, 1970, p 919-925
13. J.C. Huang and A.J. Ardell, Precipitation of Al_3Li from an Al-3.0wt.%Li Alloy and Some Properties of Al_3Li, *J. Phys.,* Vol 48 (No. C3), 1987, p 373-383
14. C.P. Blankenship, Jr. and E.A Starke, Jr., Mechanical Behavior of Double-Aged AA8090, *Metall. Trans. A,* Vol 24A, 1993, p 833-841
15. J.F. Nie, B.C. Muddle, and I.J. Polmear, The Effect of Precipitate Shape and Orientation on Dispersion Strengthening in High Strength Aluminum Alloys, *Mater. Sci. Forum,* Vol 217-222, 1996, p 1257-1262
16. Z.X. Li, R.A. Mirshams, E.A. Kenik, and P.J. Hartley, Effect of Stretch Prior to Aging on Mechanical Properties in Al-Cu-Li, 2195, Alloy, *Light Weight Alloys for Aerospace Applications IV,* E.W. Lee, W.E. Frazier, N.J. Kim, and K. Jata, Ed., The Minerals, Metals & Materials Society, 1997, p 117-127
17. B.M. Gable, A.A. Csontos, and E.A. Starke, Jr., The Role of Mechanical Stretch on the Processing-Microstructure-Property Relationships of AF/C 458, *Mater. Sci. Forum,* Vol 331-337, 2000, p 1341-1346
18. W.A. Cassada, G.J. Shiflet, and E.A. Starke, Jr., The Effect of Plastic Deformation on T_1 Precipitation, *J. Phys.*, Vol 48 (No. C3), 1987, p 397-406
19. C.P. Blankenship, Jr., E. Hornbogen, and E.A. Starke Jr., Predicting Slip Behavior in Alloys Containing Shearable and Strong Particles, *Mater. Sci. Eng.,* Vol A169, 1993, p 33-41
20. C.P. Blankenship, Jr., and E.A. Starke, Jr., Structure-Property Relationships in Al-Li-Cu-Mg-Ag-Zr Alloy X2095, *Acta Metall. Mater.,* Vol 42 (No. 3), 1994, p 845-855
21. H.K. Hardy and J.M. Silcock, The Phase Sections at 500 and 350 °C of Aluminum-Rich Aluminum-Copper-Lithium Alloys. *J. Inst. Met.,* Vol 84, 1955-56, p 423-428
22. B. Noble and G.E. Thompson, Precipitation Characteristics of Aluminum-Lithium Alloys, *Met. Sci. J.,* Vol 5, 1971, p 357-364
23. J.M. Silcock, The Structural Aging Characteristics of Aluminum-Lithium-Copper Alloys, *J. Inst. Met.,* Vol 88, 1959-1960, p 357-364
24. M.F. Ashby and R. Ebeling, On the Determination of the Number, Size, Spacing, and Volume Fraction of Spherical Second-Phase Particles from Extraction Replicas, *Trans. Metall. Soc. AIME,* Vol 236, 1966, p 1396-1404
25. W.D. Jones and P.P. Das, The Solubility of Li in Al, *J. Inst. Met.,* Vol 87, 1959, p 338-340
26. D.B. Williams and J.W. Edington, The Precipitation of δ′ (Al_3Li) in Dilute Aluminum-Lithium Alloys, *Met. Sci. J.,* Vol 9, 1975, p 529-532
27. S.F. Baumann and D.B. Williams, A New Method for the Determination of the Precipitate-Matrix Interfacial Energy, *Scr. Metall.,* Vol 18, 1984, p 611-618
28. P.L. Makin and B. Ralph, On the Aging of Aluminum-Lithium-Zirconium Alloy, *J. Mater. Sci.,* Vol 19, 1984, p 3835-3843
29. F.W. Gayle and J.B. Vander Sande, Composite Precipitates in an Al-Li-Zr Alloy, *Scr. Metall.,* Vol 18, 1984, p 473-478
30. E.E. Underwood, *Quantitative Stereology*, Addison-Wesley, 1970
31. J.E. Hilliard, The Counting and Sizing of Particles in Transmission Microscopy, *Trans. Metall. Soc. AIME,* Vol 224, 1962, p 906-917
32. A.K. Vasudevan and K. Sadananda, Classification of Fatigue Crack Growth Behavior, *Metall. Mater. Trans.,* Vol 26A (No. 5), 1995, p 1221-1234
33. C.W. Corti, P. Cotterill, and G.A. Fitzpatrick, The Evaluation of the Interparticle Spacing in Dispersion Alloys, *Int. Metall. Rev.,* Vol 19, 1974, p 77-88
34. P.L. Goldsmith, The Calculation of True Particle Size Distributions From the Size Observed in a Thin Slice, *Br. J. Appl. Phys.,* Vol 18, 1967, p 813-830
35. J.M.G. Crompton, R.M. Wagnhorne, and G.B. Brook, The Estimation of Size Distribution and Density Precipitates From Electron Micrographs of Thin Foils, *Br. J. Appl. Phys.,* Vol 17, 1966, p 1301-1305
36. E. Hornbogen and K.-H. Zum Gahr, Microstructure and Fatigue Crack Growth in a γ- Fe-Ni-Al Alloy, *Acta Metall.,* Vol 24, 1976, p 581-592
37. K.V. Jata and E.A. Starke, Fatigue Crack Growth and Fracture Toughness Behavior of an Al-Li-Cu Alloy, *Metall. Trans.,* Vol 17A, 1986, p 1011-1026